Nano World Journal

http://dx.doi.org/10.17756/nwj.2015-009

Review Article

Open Access

Protein Micro-Crystallography: Nanotechnology Challenges Ahead

Christian Riekel

ESRF-The European Synchrotron, CS40220, F-38043 Grenoble Cedex 9, France

Correspondence to:
Dr. Christian Riekel
European Synchrotron Radiation Facility
Experiments Division
Complex Systems and Biomedical Sciences Group
B.P.220, F-38043 Grenoble Cedex, France
Tel: 003347688205
Fax: 003476882542
E-mail: riekel@esrf.fr

Received: September 14, 2015
Accepted: October 5, 2015
Published: October 9, 2015

Citation: Riekel C. 2015. Protein Micro-Crystallography: Nanotechnology Challenges Ahead. *NanoWorld J* 1(3): 73-78.

Published by United Scientific Group

Abstract

The status and prospects of protein microcrystallography (MPX) at high brilliance synchrotron radiation sources are reviewed. We discuss emerging trends in miniaturizing sample environments for serial crystallography (SX) experiments allowing manipulation and positioning of biological objects down to nanoscale dimensions with low contact forces.

Keywords

Synchrotron radiation, X-ray free electron laser, Protein microcrystallography, Serial crystallography, Nanotechnology, Sample environment

Abbreviations

MPX: Protein Microcrystallography; SR: Synchrotron Radiation; SX: Serial Crystallography; SFX: Serial Femtosecond Crystallography; SSX: Synchrotron Serial Crystallography; XFEL: X-ray Free Electron Laser; TMV: Tobacco Mosaic Virus

Introduction

Protein microcrystallography (MPX) at 3rd generation synchrotron radiation (SR) sources [1,2] has provided access to structures which are difficult to crystallize such as amyloids [3] or membrane proteins [4,5]. Technical and scientific progress is dominated by the development of more and more brilliant X-ray sources allowing recording diffraction patterns from increasingly smaller crystals in a shorter time. X-ray free electron laser sources (XFEL), such as the Linac Coherent Light Source (LCLS, Stanford, California, USA) have profoundly modified MPX [6, 7]. Indeed, femtosecond X-ray flashes from XFELs allow obtaining quasi radiation-damage-free diffraction data from nm-sized crystallites in a hit-and-destroy mode [7-9]. This has resulted in serial femtosecond crystallography (SFX) techniques based on the merging of patterns due to hits from thousands of crystallites [10]. Indeed, a microjet injector containing photosystem I crystallites down to 200 nm size was used for the first SFX experiment (Figure 1) [9, 11]. For an overview on other SFX flow-injectors and fixed target supports see: [12]. The limited availability of XFELs provides, however, a drive for optimizing SR-MPX beam lines and using both types of sources in a complementary way. Indeed, SR-MPX provides currently access to crystallite volumes down to a few μm^3 [1, 2, 13] while nm^3 volumes have become accessible at XFELs [9]. Radiation-free XFEL data collection is a dream-come-true for protein crystallographers. SR-experiments provide, however, more flexibility for in-situ sample environments such as crystallization plates or microfluidic devices. Special care has, however, to be taken to minimize radiation damage in SR-MPX experiments.

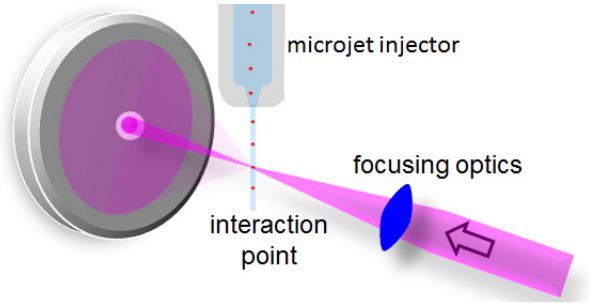

Figure 1: Schematic SFX setup. The X-ray beam is focused by mirror or refractive lens X-ray optics onto the interaction point where a slush of crystallites from a microjet injector is crossed with the X-ray beam [9]. A diffraction pattern is recorded on the detector every time a crystallite is hit by an X-ray flash.

In the following we will first review several emerging trends for SR-MPX with beam sizes from the µm- to the nm-range and then highlight the potential of advanced sample environments. Rather than being exhaustive we will focus on selected on-chip sample environments and low contact-force manipulation derived from nanobiotechnology tools and techniques [14]. The term "MPX" will be used independently of the X-ray beam size.

Sources and Beamlines

A comparison of the brilliance (corresponding to the photon concentration; also called spectral brightness) of 3rd generation SR sources shows the progress in maximum brilliance for the most recent SR sources (e.g. MAX IV, [15] NSLS II [16]) which are based on advanced magnet lattice designs (Figure 2A). The correlation of focal spot size and maximum flux density of a number of SR-MPX beam lines worldwide reveals that the most advanced SR sources aim for a particularly high (monochromatic) flux density of ~10^{13} photons/(s, µm^2) for an ~1 µm^2 focus (Figure 2B); ($FMX_{NSLS\ II}$ beamline). The drive towards higher SR brilliances is, however, continuing. Indeed, the brilliance depends on the horizontal and vertical emittance ($\varepsilon_{hor,vert}$) of the electron beam in a storage ring which is the product of its size ($\delta_{hor,vert}$) and divergence ($\delta'_{hor,vert}$). The emittance can be reduced by a compression of the electron beam up to its theoretical limit when electron diffraction effects set in. This limit defines a 4th generation ("diffraction limited") SR source [17]. Indeed, the ESRF storage ring, which has started operation in 1992, will be upgraded until 2020 into a close-to 4th generation SR-source by a change of its magnetic lattice (ESRF II; dashed curve in (Figure 1A) [18]. Several other major 3rd generation SR sources (e.g. APS and SPring8) will follow this example. This will favor in particular "brilliance-hungry" experimental techniques, currently proposed only at few SR beamlines worldwide. Examples are sub-µm SR-MPX [19, 20] (e.g. $ID13_{ESRF}$); (Figure 2B) and time-resolved SR-MPX based on picoseconds X-ray flashes using an undulator harmonics ("pink" beam), a technique currently developed only for larger SR beam foci [21]. One can estimate that a "pink" SR-MPX beam line would reach at ESRF-II the 10^{16} flux density range.

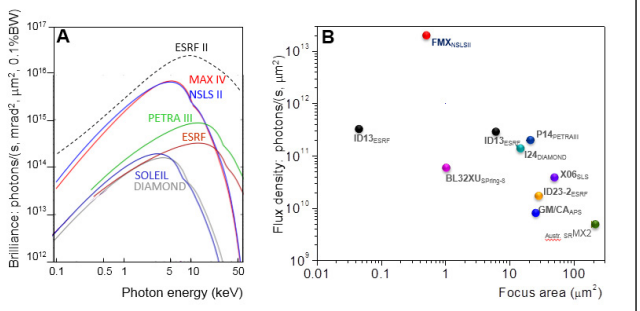

Figure 2 A: Overview on the brilliance for selected SR-sources including undulators (Adapted from: [18, 52]; BW: band width). Relevant values (same units) for CXI beamline at the LCLS-XFEL: maximum brilliance: 2x10^{27}; average brilliance: 4x10^{25} (30 Hz) [6]. **B:** Maximum peak flux density in the 8-13 keV range versus focal spot area for selected SR-MPX beamlines using monochromatic beams (based on values from April 2015; $FMX_{NSLS\ II}$: simulated; operational in 2016). $ID13_{ESRF}$ is currently the only beamline providing both µm- and sub-µm beams for SR-MPX (part-time use). SR-sources: Diamond: Oxford, UK; Soleil: Saclay, France; ESRF: Grenoble; France, Petra III: Hamburg, Germany; NSLS II: Brookhaven, USA; MAX IV: Lund, Sweden; APS: Chicago, USA; SLS: Villigen, Switzerland; SPring-8: Harima, Japan; Australian SR: Clayton, Australia.

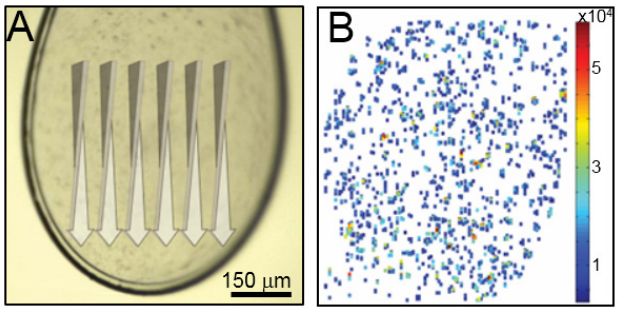

Figure 3 A: Schematic design of SSX based on helical line-scans projected on a cryogenic loop filled with a slush of needle-like TbCatB crystallites [13]. **B:** Raster-diffraction ("Heat") map of crystallites in the cryogenic loop after software preselection. The color bar codes correspond to the average intensity of the Bragg peaks in each diffraction pattern as an indication of the diffraction strength of each pattern (Adapted from: [13]).

Synchrotron Radiation Serial Crystallography (SSX)

SSX on cryo frozen samples is becoming an automated data collection workflow at SR-MPX beam lines [22]. It has first been demonstrated for Trypanosoma brucei procathepsin B (TbCatB) crystallites of about 2 µm average size using helical raster-rotation scans to obtain "classical" rotation patterns and distribute the radiation dose (Figure 3A) [13]. The hits are displayed in a "heat map" scaled to the overall diffraction strength in each pattern (Figure 3B). The 0.3 nm resolution structure based on 426 patterns from 80 crystallites is of similar quality for the main-chain features as the 0.21 nm resolution SFX study based on 2.9x10^5 patterns [23].

The statistical treatment of SSX data based on the hierarchical cluster analysis [24] allows readily matching complementary patterns from many different crystallites into groups [25]. A potential target for this approach is exploring experimentally the mosaic block (called here: micro-domain) model (Figure 4A) [26]. We note that individual micro-domains in the bulk of a well-ordered protein crystal are not readily accessible to a diffraction experiment. The combination of laser-microdissection and solvent-induced micro-fragmentation allows, however, physically separating a

crystal into micro-domains as shown for a lysozyme crystal generated by the Langmuir-Blodgett nanotemplate technique (Figures 4B & 4C) [19, 27]. A raster-scan heat map obtained with a 400 nm beam of a micro-fragmented lysozyme crystal in a cryogenic loop revealed two micro-domains (Figure 4D). Rotation patterns were collected from each micro-domain and their 3D structures refined [19].The results suggest that laser-induced microcavitation and solvent-induced micro-domain separation do not introduce lattice distortions. SSX of a sufficiently large set of micro-domains from a micro-fragmented crystal could possibly provide information on the variability of crystallographic parameters or allow picking out crystalline micro-domains for highly mosaic crystals.

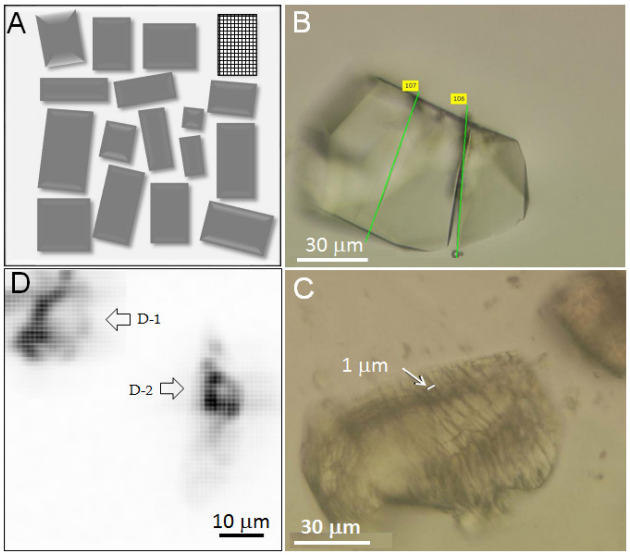

Figure 4 A: Idealized mosaic block model showing schematically a regular lattice for one micro-domain (Adapted from: [26]). **B:** Lysozyme crystal during laser microdissection along green lines [19]. **C:** Same crystal after micro-fragmentation in glycol/water solution. **D:** The heat map of a micro-fragmented lysozyme crystal in a cryogenic loop reveals 2 micro-domains based on the 600 (D-1) and 200 (D-2) reflection intensities (Adapted from: [19]).

SSX at room temperature is a challenge for SR-MPX due to radiation damage effects although secondary radiation damage becomes negligible for crystallites in the µm-range [28, 29]. A number of room temperature sample environments tested at SR-MPX beam lines have been initially developed for SFX experiments [12, 30-33]. Such experiments are generally performed without crystal rotation. Probing a capillary filled with a lysozyme crystallite flush [34] would, however, not be possible at an XFEL due to an immediate destruction of the capillary walls. The SSX lysozyme structure was refined to 0.21 nm based on about $4x10^4$ patterns using about 250 mg protein. Increasing the flow-density by a liquid crystalline polymer (LCP) phase allows reducing the protein consumption to the 1 mg range. Indeed, an LCP matrix filled with about 30 µm size bacteriorhodopsin crystallites was extruded into air and probed by SSX [35].This membrane protein structure was refined to 0.24 nm resolution. A similar protein consumption has been obtained for randomly distributed crystallites on a fixed target by raster-scan SFX [32]. The same approach was used for SSX with micro- and nanobeams on a slurry of lysozyme crystallites contained between Si_3N_4 membranes (Figure 5A & 5B). The main-chain lysozyme structure was only slightly affected by radiation damage and there was practically no difference for the two beam sizes. The particularly high radiation dose for nanobeam SSX of 29 MGy/crystallite was tentatively attributed to a lag phase [20].The availability of up to KHz framing rate, zero readout noise pixel detectors -such as the EIGER detector from DECTRIS®- will allow further reducing protein consumption in SSX experiments.

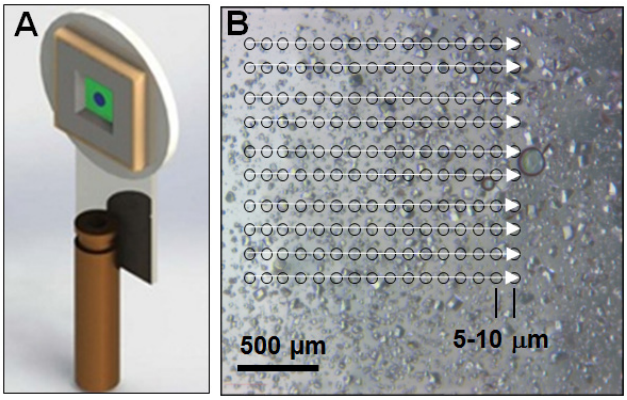

Figure 5 A: Lysozyme crystallite slush, sealed between two Si_3N_4 membranes within Si-frames and supported by a washer. **B:** Optical image of lysozyme slush. The circles indicate schematically the mesh of raster-steps with a step-width of 5 or 10 µm. The scan sequence is indicated by white arrows starting at the top left corner (Adapted from: [20]).

On-Chip Sample Environments and Low Contact-Force Manipulation

Sample environments for SX experiments have to cope with the manipulation of µm- to nm-sized biological objects which suggests exploring the use of nanobiotechnology tools and techniques. Furthermore, deterministic positioning of objects in the beam allows reducing the sample consumption and therefore also the data collection time by increasing the crystallites hit rate. The fragility of many proteins, such as membrane proteins, also requires manipulation and positioning with low contact forces. Ideally, self-assembly into crystalline objects and their localization should be done in the same sample environment. The strategies discussed below are likewise of interest for SFX and SSX. A more detailed overview on different positioning & manipulation techniques will be provided elsewhere [36].

Sorting of objects on structured substrates

The aim is to preposition objects on a structured surface so that a high hit rate can be obtained by mesh-scans with a step size corresponding to the separation of the objects. An example for this is provided by a silicon chip with a hole-pattern etched into a 10 µm membrane by photolithography techniques (Figure 6A) [37]. Evaporating a droplet containing a slush of crystallites on the chip allows immobilizing individual crystallites in the down to 1 µm diameter holes by capillary action (Figure 6B).

Chips with nanofabricated pillared superhydrophobic surfaces are an alternative possibility for exploiting

localization of objects during droplet evaporation (Figure 6C & 6D) [38]. The shrinkage of a water or dilute solute droplet during evaporation results in a wetting transition with liquid entering the gaps between the pillars [38]. At higher solute concentrations, a viscous protein layer is formed at the droplet rim by convective-flow mediated mass transport during evaporation. The reduced molecular mobility at the rim can result in self-assembly and the formation of 1D or 2D

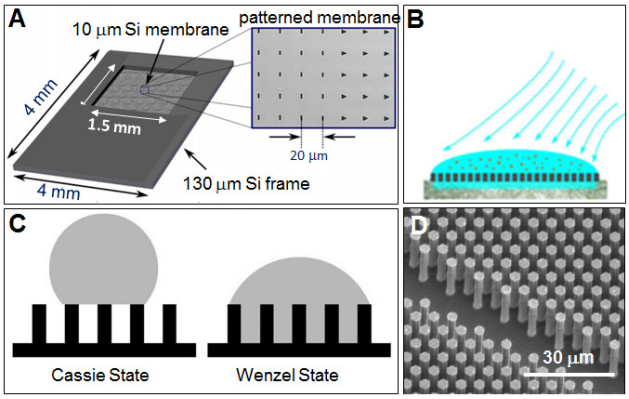

Figure 6 A: Schematic design of Si chip containing a 10 µm thick patterned Si-membrane (Adapted from: [37]). **B:** Schematic picture of evaporating droplet on patterned Si-membrane. Liquid is entering the holes of the membrane by capillary action and pulls along crystallites from the slush. **C:** Schematic design of droplet transition from superhydrophobic (Cassie) to wetting (Wenzel) state. **D:** SEM image of pillared superhydrophobic surfaces obtained by etching a silicon wafer [38].

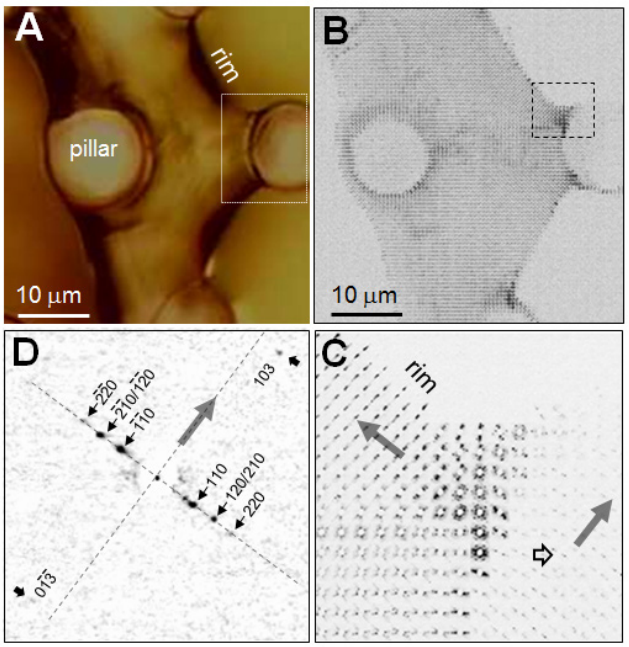

Figure 7 A: Optical image of TMV coffee-ring type residue on pillared superhydrophobic chip [41]. **B:** Heat map of residue shown in (A) with 500 nm step increments. The angular range of the individual patterns is limited to the inner-most reflections. The highly binned patterns simulate average Bragg peak intensities (see Figure 3B). Note the scattering of a thin layer covering partially the pillar which is also visible in (A). **C:** Zoom into rectangular dashed area in (B) revealing domains defined by patterns with the same texture. **D:** Individual pattern from a position on top of the pillar with the thin layer (open arrow in C). The reflections have been indexed for a hexagonal primitive TMV lattice with a=b=17.2 nm, c=6.73 nm, γ=1200 [43]. The orientation of the TMV nanorods is indicated in C, D by grey arrows.

morphologies [39, 40]. Indeed, a solution of rod-like tobacco mosaic virus (TMV) particles of 300 nm length and 18 nm diameter forms a coffee-ring type layer on the pillars (Figure 7A) [40, 42]. Raster-diffraction with a 170x130 nm^2 beam reveals micro-domains on and between the pillars with the nanorods axes aligned more or less parallel to the rim and pillar surface (Figure 7B & 7C). Single crystalline features, already noted in a TMV microbeam study [43], are apparent in a pattern from the residue of the retracting layer on top of a pillar (Figure 7A & 7B). The best resolution of 1.6 nm obtained until now for a TMV coffee-ring residue [43] cannot yet compete with the 0.29 nm resolution obtained by X-ray fiber diffraction on much larger scattering volumes [44]. Improving the resolution of self-assembled TMV particles on artificially structured substrates will be an interesting challenge.

Manipulation and assembly of objects with ultralow contact forces

Objects from nm to several 10th of µm dimensions can be trapped by pN optical forces generated by milliwatts of visible laser light focused through a microscope objective onto the object, such as crystallites in a capillary (Figure 8A) [45, 49]. The optical field reduces random motion due to Brownian forces, allowing raster-scans of trapped objects by microPX techniques [48, 49]. The laser beam can be split holographically into multiple traps [46]. Indeed, an about 30 µm insulin crystal could be kept in a fixed position by three holographic traps and its radiation damage explored in-situ using a dedicated optical tweezers setup (Figure 8B) [49]. Radiation damage appeared only beyond about 50 ms local exposure suggesting that SSX based on raster-rotation scans would be feasible for larger microcrystals provided that the separation of the scan points is a few µm, i.e. corresponding to the range of secondary radiation damage due to X-ray induced photoelectrons [50].

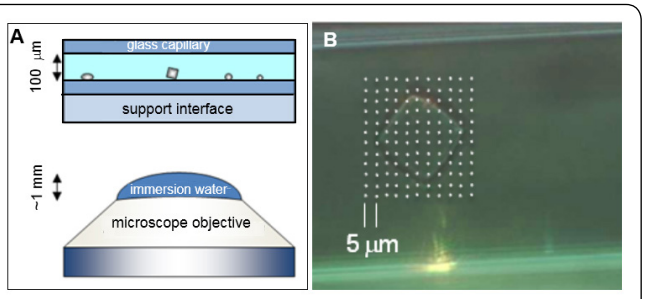

Figure 8 A: Schematic optical tweezers sample environment. A 100 µm diameter capillary containing crystallites is adapted to an immersion objective which focuses the laser beam into the capillary. **B:** Optical microscopy image of a trapped insulin crystal with a superimposed raster-scan grid in a 100 µm inner diameter capillary (Adapted from; [49]). The size of the grid-points corresponds to the beam size of about 1 µm. The beam direction is along the crystallographic [001] direction. The laser beam is visible as a yellow trace on the lower capillary wall.

Materials used for sample supports or confinement

In order to cope with objects of very low scattering power, sample supports and confining walls have to have ultralow background scattering and X-ray absorption. Indeed, scattering from a 10 µm single-crystalline silicon membrane [37] is very low for a transmission of ~97 % at λ~0.1 nm wavelength. The

transmission is >99.8% for a 1 μm thick Si_3N_4 membrane used in a superhydrophobic chip [41]. This material is, however, very fragile and future sample supports should rather be based on few atomic layers thick graphene which has virtually 100 % transmission and no background scattering [51].

Conclusion

"Pushing the limits of protein crystallography to smaller crystals and smaller beam sizes requires the integration of more and more nanotechnology into a MPX beam line and annex laboratories" [1]. The examples reviewed in this article with an emphasis for on-chip sample environments support this statement and suggest R&D opportunities related to nanobiotechnology tools and techniques.

Acknowledgements

Helpful discussions with A. Accardo, F. De Angelis and G. Marinaro (IIT-Genova), E. Pechkova (Genova University), C. Nicolini (Fondazione ELBA), M. Burghammer, A. Popov, S.C. Santucci (ESRF-Grenoble), J.P. Colletier and N. Coquelle (IBS-Grenoble) are gratefully acknowledged.

References

1. Riekel C, Burghammer M, Popov D. 2011. Protein Micro- and Nanocrystallography using Synchrotron Radiation. In: Pechkova E and Riekel C (eds) Synchrotron Radiation and Structural Proteomics, Pan Stanford Series on Nanobiotechnology, CRC (Taylor & Francis), Boca Raton, FL, USA, pp: 3-30.
2. Smith JL, Fischetti RF, Yamamoto M. 2012. Micro-Crystallography Comes of Age. *Curr Opin Struct Biol* 22(5): 602-612. doi: 10.1016/j.sbi.2012.09.001
3. Nelson R, Sawaya MR, Balbirnie M, Riekel C, Grothe R, et al. 2005. Structure of the Cross-b Spine of Amyloid-Like Fibrils. *Nature* 435: 773-778. doi: 10.1038/nature03680
4. Cherezov V, Rosenbaum DM, Hanson MA, Thian FS, Kobilka TS, et al. 2007. High-Resolution Crystal Structure of an Engineered Human β2-Adrenergic G Protein–Coupled Receptor. *Science* 318(5854): 1258-1265. doi: 10.1126/science.1150577
5. Rasmussen SGF, Choi HJ, Rosenbaum DM, Kobilka TS, Thian FS, et al. 2007. Crystal Structure of the Human β_2 Adrenergic G-Protein-Coupled Receptor. *Nature* 450(7168): 383-387. doi: 10.1038/nature06325
6. Boutet S, Williams GJ. 2010. The Coherent X-ray Imaging (CXI) instrument at the Linac Coherent Light Source (LCLS). *New J Phys* 12: 035024. doi: 10.1088/1367-2630/12/3/035024
7. Schlichting I. 2015. Serial Femtosecond Crystallography: the First Five Years. *IUCrJ* 2(2): 246-255. doi: 10.1107/S205225251402702X
8. Neutze R, Wouts R, van der Spoel D, Weckert E, Hadju J. 2000. Potential for Biomolecular Imaging with Femtosecond X-Ray Pulses. *Nature* 406: 753-757. doi: 10.1038/35021099
9. Chapman HN, Fromme P, Barty A, White TA, Kirian RA, et al. 2011. Femtosecond X-Ray Protein Nanocrystallography. *Nature* 470(7332): 73-77. doi: 10.1038/nature09750
10. White TA, Barty A, Stellato F, Holton JM, Kirian RA, et al. 2013. Crystallographic Data Processing for Free-Electron Laser Sources. *Acta Crystallogr D Biol Crystallogr* 69(7): 1231-1240. doi: 10.1107/S0907444913013620
11. DePonte DP, Weierstall U, Schmidt K, Starodub D, Spence JCH, et al. 2008. Gas Dynamic Virtual Nozzle for Generation of Microscopic Droplet Streams. *J Phys D Appl Phys* 41: 195505.
12. Muniyappan S, Kim SO, Ihee H. 2015. Recent Advances and Future Prospects of Serial Crystallography using XFEL and Synchrotron X-Ray Sources. *Bio Design* 3(2): 98-110.
13. Gati C, Bourenkov G, Klinge M, Rehders D, Stellato, F, et al. 2014. Serial Crystallography on In Vivo Grown Microcrystals using Synchrotron Radiation. *IUCrJ* 1(2): 87-94. doi: 10.1107/S2052252513033939
14. Gazit E, Mitraki A. 2013. Plenty of Room for Biology at the Bottom. An Introduction into Bionanotechnology (World Scientific). doi: 10.1142/9781848169319_bmatter
15. Tavares PF, Leemann SC, Sjoestroem M, Andersson A. 2014. The MAX IV Storage Ring Project. *J Synchr Rad* 21(5): 862-877. doi: 10.1107/S1600577514011503
16. National Synchrotron Light Source II: Wikipedia
17. Eriksson M, Van der Veen JF, Quitmann C. 2014. Diffraction-Limited Storage Rings – a Window to the Science of Tomorrow. *J Synchr Rad* 21(5): 837-842. doi: 10.1107/S1600577514019286
18. Dimper R, Reichert H, Raimondi P, Ortiz LS, Sette F, et al. 2015. The Orange Book: ESRF Upgrade Programme Phase II (2015-2022) - Technical Design Study. The European Synchrotron, Grenoble.
19. Pechkova E, Belmonte L, Riekel C, Popov D, Koenig C, et al. 2013. Laser-Microdissection of Protein Crystals Down to Submicron Dimensions. *J Nanomed Nanotech* S15: 002. doi: 10.4172/2157-7439
20. Coquelle N, Brewster AS, Kapp U, Shilova A, Weinhausen B, et al. 2015. Raster-Scanning Serial Protein Crystallography using Micro and Nano-Focused Synchrotron Beams. *Acta Crystallogr D Biol Crystallogr* 71(5): 1184-1196. doi: 10.1107/S1399004715004514
21. Kim TK, Lee JH, Wulff M, Kong Q, Ihee H. 2009. Spatiotemporal Kinetics in Solution Studied by Time-Resolved X-Ray Liquidography (Solution Scattering). *ChemPhysChem* 10(12): 1958-1980. doi: 10.1002/cphc.200900154
22. Zander U, Bourenkov G, Popov AN, de Sanctis D, Svensson O, et al. 2015. MeshAndCollect: an Automated Multi-Crystal Data-Collection Workflow for Synchrotron Macromolecular Crystallography Beamlines. *Acta Crystallogr D Biol Crystallogr* 71(Pt 11): 2328-2343. doi: 10.1107/S1399004715017927
23. Redecke L, Nass K, DePonte DP, White TA, Rehders D, et al. 2013. Natively Inhibited Trypanosoma Brucei Cathepsin B Structure Determined by Using an X-ray Laser. *Science* 339(6116): 227-230. doi: 10.1126/science.1229663
24. Giordano R, Leal RM, Bourenkov GP, McSweeney S, Popov AN. 2012. The Application of Hierarchical Cluster Analysis to the Selection of Isomorphous Crystals. *Acta Crystallogr D Biol Crystallogr* 68(6): 649-658. doi: 10.1107/S0907444912006841
25. Svensson O, Malbet-Monaco S, Popov A, Nurizzoa D, Bowler MW. 2015. Fully Automatic Characterization and Data Collection from Crystals of Biological Macromolecules. *Acta Crystallogr D Biol Crystallogr* 71(8): 1757-1767. doi: 10.1107/S1399004715011918
26. Nave C. 1999. Matching X-Ray Source, Optics and Detectors to Protein Crystallography Requirements. *Acta Crystallogr D Biol Crystallogr* 55: 1663-1668. doi: 10.1107/S0907444999008380
27. Pechkova E, Nicolini C. 2003. Proteomics and Nanocrystallography. Kluwer Academic Press, NY, USA. doi: 10.1007/978-1-4615-0041-4
28. Nave C, Hill MA. 2005. Will Reduced Radiation Damage Occur with Very Small Crystals? *J Synchotron Rad* 12: 299-303. doi: 10.1107/S0909049505003274
29. Cowan JA, Nave C. 2008. The Optimum Conditions to Collect X-Ray Data from Very Small Samples. *J Synchrotron Rad* 15(5): 458-462. doi: 10.1107/S0909049508014623
30. Liu W, Wacker D, Gati C, Han GW, James D, et al. 2013. Serial Femtosecond Crystallography of G Protein–Coupled Receptors. *Science* 342(6165): 1521-1524. doi: 10.1126/science.1244142
31. Weierstall U, James D, Wang C, White TA, Wang D, et al. 2014. Lipidic Cubic Phase Injector Facilitates Membrane Protein Serial

Femtosecond Crystallography. *Nat Commun* 5: 3309. doi: 10.1038/ncomms4309

32. Hunter MS, Segelke B, Messerschmidt M, Williams GJ, Zatsepin NA, et al. 2014. Fixed-Target Protein Serial Microcrystallography with an X-Ray Free Electron Laser. *Sci Rep* 4: 6026. doi: 10.1038/srep06026
33. Caffrey M, Li D, Howe N, Shah ST. 2014. "Hit and Run" Serial Femtosecond Crystallography of a Membrane Kinase in the Lipid Cubic Phase. *Phil Trans R Soc London B* 369(1674): 20130621. doi: 10.1098/rstb.2013.0621
34. Stellato F, Oberthur D, Liang M, Bean R, Gati C, et al. 2014. Room-Temperature Macromolecular Serial Crystallography Using Synchrotron Radiation. *IUCrJ* 1(4): 204-212. doi: 10.1107/S2052252514010070
35. Nogly P, James D, Wang D, White TA, Zatsepin N, et al. 2015. Lipidic Cubic Phase Serial Millisecond Crystallography using Synchrotron Radiation. *IUCrJ* 2(2):168-176. doi: 10.1107/S2052252514026487
36. Accardo A, Graceffa R, Riekel C. Deterministic Delivery of Ultrasmall Volumes of Biological Materials (in preparation).
37. Roedig P, Vartiainen I, Duman R, Panneerselvam S, Stübe N, et al. 2015. A Micro-Patterned Silicon Chip as Sample Holder for Macromolecular Crystallography Experiments with Minimal Background Scattering. *Sci Rep* 5: 10451. doi: 10.1038/srep10451
38. Accardo A, DiFabrizio E, Limongia T, Marinaro G, Riekel C. 2014. Probing Droplets on Superhydrophobic Surfaces by Synchrotron Radiation Scattering Techniques. *J Synchrotron Radiat* 21(4): 643-653. doi: 10.1107/S1600577514009849
39. Gentile F, Moretti M, Limongi T, Falqui A, Bertoni G, et al. 2012. Direct Imaging of DNA Fibers: The Visage of Double Helix. *Nano Lett* 12(12): 6453-6458. doi: 10.1021/nl3039162
40. Marinaro G, Burghammer M, Costa L, Dane T, de Angelis F, et al. 2015. Directed Growth of Virus Nanofilaments on a Superhydrophobic Surface. *ACS Appl Mater Interfaces* 7(23): 12373–12379. doi: 10.1021/am507509z
41. Marinaro G, Accardo A, De Angelis F, Dane T, Weinhausen B, et al. 2014. A Superhydrophobic Chip based on SU-8 Photoresist Pillars Suspended on a Silicon Nitride Membrane. *Lab Chip* 14(19): 3705-3709. doi: 10.1039/c4lc00750f
42. Marinaro G. 2015. Contributions to Modeling and Applications of Superhydrophobic Surfaces for Self-Assembly of Biological Materials. PhD Thesis, University of Genova, Genova, Italy.
43. Gebhardt R, Teulon JM, Pellequer JL, Burghammer M, Colletier JP, et al. 2014. Virus Particle Assembly into Crystalline Domains Enabled by the Coffee Ring Effect. *Soft Matter* 10(30): 5458-5462. doi: 10.1039/c4sm00414k
44. Namba K, Pattanayek R, Stubbs G. 1989. Visualization of Protein-Nucleic Acid Interactions in a Virus. Refined Structure of Intact Tobacco Mosaic Virus at 2.9 A Resolution by X-Ray Fiber Diffraction. *J Mol Biol* 208(2): 307-325.
45. Ashkin A, Dziedzic JM. 1971. Optical Levitation by Radiation Pressure. *Appl Phys Lett* 19: 283-285. doi: 10.1063/1.1653919
46. Grier DG. 2003. A Revolution in Optical Manipulation. *Nature* 424: 810-816. doi: 10.1038/nature01935
47. Neuman KC, Block SM. 2004. Optical Trapping. *Rev Sci Instrum* 75(9): 2787-2809. doi: 10.1063/1.1785844
48. Santucci SC, Amenitsch H, Cojoc D, Riekel C. 2011. Optical Tweezers for Touchless Sample Manipulation in Synchrotron Radiation Experiments. In: Pechkova E and Riekel C (eds) Synchrotron Radiation and Structural Proteomics, Pan Stanford Series on Nanobiotechnology, CRC (Taylor & Francis), Boca Raton, FL, USA, pp 183–211.
49. Santucci SC, Cojoc D, Amenitsch H, Marmiroli B, Sartori B, et al. 2011. Optical Tweezers for Synchrotron Radiation Probing of Trapped Biological and Soft Matter Objects in Aqueous Environments. *Anal Chem* 83(12): 4863-4870. doi: 10.1021/ac200515x
50. Cole A. 1969. Absorption of 20-eV to 50,000-eV Electron Beams in Air and Plastic. *Radiat Res* 38(1): 7-33.
51. Gruner SM, Lattman EE. 2015. Biostructural Science Inspired by Next-Generation X-Ray Sources. *Annu Rev Biophys* 44: 33-51. doi: 10.1146/annurev-biophys-060414-033813
52. Wallen E. 2011. Comparison of the Brilliance Limit between MAX IV 3 GeV Ring and NSLS II Low Beta Straights Using the Same Undulator Technique. in Internal Note 20111110 (MAX IV Lab).